MCAT Institute
Progress Report
92-007

P- 17

NUMERICAL STUDIES OF THE FLUID AND OPTICAL FIELDS ASSOCIATED WITH COMPLEX CAVITY FLOWS

Christopher A. Atwood

April 1992

NCC2-677

MCAT Institute
3933 Blue Gum Drive
San Jose, CA 95127

CASI

Numerical Studies of the Fluid and Optical Fields Associated with Complex Cavity Flows

Christopher A. Atwood

Numerical solutions for the flowfields about several cavity configurations have been computed using the Reynolds-averaged Navier-Stokes equations. Comparisons between numerical and experimental results are made in two-dimensions for free shear layers and a rectangular cavity, and in three-dimensions for the transonic aero-window problem of the Stratospheric Observatory for Infrared Astronomy (SOFIA). Results show that dominant acoustic frequencies and magnitudes of the self-excited resonant cavity flows compare well with experiment. In addition, solution sensitivity to artificial dissipation and grid resolution levels are determined. Furthermore, optical path distortion due to the flow field is modelled geometrically and is found to match the experimental trend.

The fluid field was computed using a diagonalized scheme within an overset mesh framework, thus combining efficiency with geometric versatility. An existing code, OVERFLOW, was utilized with the additions of characteristic boundary condition and output routines required for reduction of the unsteady data. The time history of the flow was transformed to the frequency domain using Fourier methods allowing for specification of windowing functions. Solution of optical propagation through the shear layer was determined via geometric optics, including the effects of refraction. The newly developed code is directly applicable to a generalized three-dimensional structured grid zone.

Details of the numerical method and the results obtained are described in detail in Appendix A.

APPENDIX A

AIAA-92-0656

Flowfield Simulation about the SOFIA Airborne Observatory

Christopher A. Atwood
MCAT Institute, NASA Ames Research Center

and

William R. Van Dalsem
NASA Ames Research Center
Moffett Field, CA 94035-1000

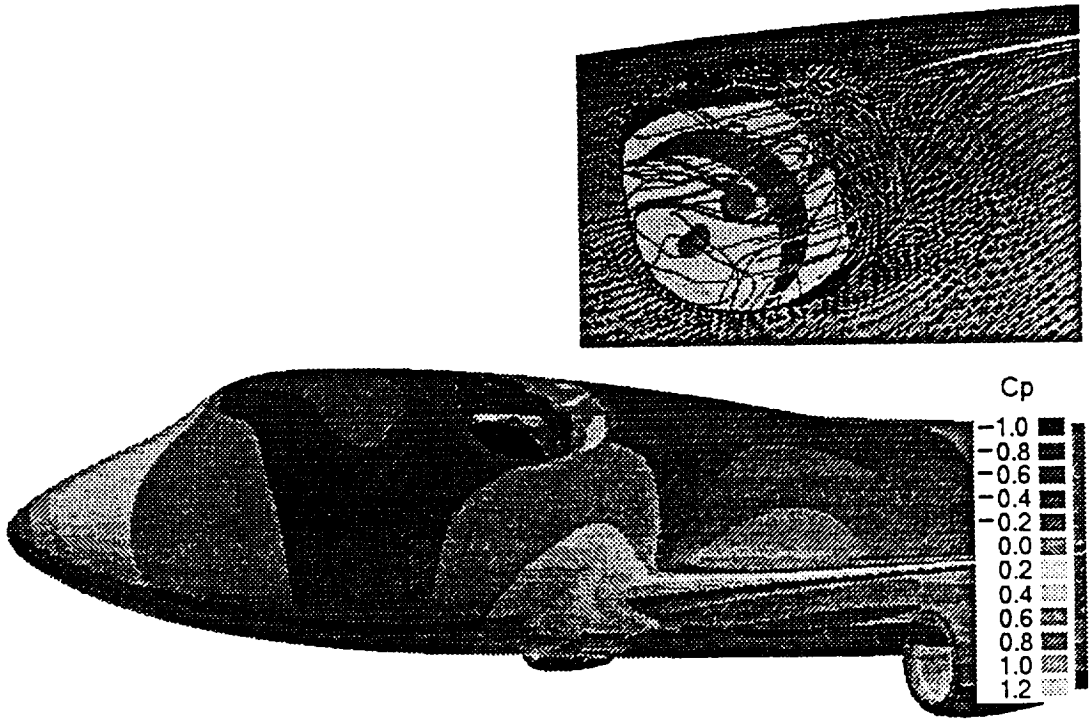

30th Aerospace Sciences Meeting & Exhibit
January 6-9, 1992 / Reno, NV

Flowfield Simulation about the SOFIA Airborne Observatory

Christopher A. Atwood* and William R. Van Dalsem†
NASA Ames Research Center, Moffett Field, California 94035-1000

Abstract

The Reynolds averaged Navier-Stokes equations have been applied to Stratospheric Observatory For Infrared Astronomy (SOFIA) configurations. Comparisons between numerical and experimental results are made in two-dimensions for free shear layers and a rectangular cavity, and in three-dimensions for simplified SOFIA geometries. Dominant acoustic behaviour of the cavity flows compare well with experiment. The sensitivity of the solutions to changes in grid cell size and artificial dissipation levels are shown. Furthermore, optical path distortion due to the flow field is modelled using geometrical constructs. The results demonstrate the viability and usefulness of the present computational method for this class unsteady applications.

Nomenclature

$\mathbf{i}, \mathbf{j}, \mathbf{k}$	Cartesian unit vectors
J	coordinate transformation Jacobian
M	Mach number
n	absolute index of refraction
$\mathbf{n}$	surface normal
p	static pressure
Q	vector of dependent variables
Re	Reynolds number
$\mathbf{r}$	position vector
t	time or parametric ray coordinate
$\mathbf{t}$	tangential direction
u, v, w	Cartesian velocity components or parametric surface coordinates
α	angle of attack
β	Gladstone-Dale constant
ν	Courant-Friedrichs-Lewy number
ρ	density
σ	measure of shear layer spread rate or wavefront distortion
θ	angle subtending the ray and normal
ξ, η, ζ	curvilinear space coordinates

Subscripts

i, j, k	ξ, η, ζ direction indices
i, n, r	incident, normal, refracted
STP	standard temperature and pressure
t	tangential or turbulent quantity
∞	freestream quantity

Introduction

The SOFIA will be a three meter class Cassegrain telescope which utilizes a Boeing 747SP as an observation platform. An artist's concept of the observatory is shown in Fig. 1. This project is currently a cooperative effort between the United States' NASA and Germany's DARA. Airborne systems of this type offer capabilities which augment land and space-based options. First, the mission flexibility of a long-range mobile platform lends astronomers freedom to investigate transient astronomical phenomena on a global basis. Second, atmospheric attenuation of some wavelengths of interest provide motivation for a platform which operates above the tropopause. Third, the cost of maintaining and upgrading observation technologies is lower than would be incurred with an orbiting configuration.

Nevertheless, the use of an aircraft-based observatory presents some challenges. The limited bandwidth of solid materials in the infrared frequency ranges of interest preclude their use as a window. Therefore, the telescope cavity must remain open to the freestream. Wind tunnel tests have shown that violent shear layer oscillations with concomitantly dangerous levels of acoustic loading occur for untreated open cavity configurations.[1] Here the term untreated indicates that the cavity shape is rectangular. Therefore, there is a need to develop cavity flow control treatments to suppress the flow unsteadiness. To reduce the risk of injury to the crew or damage to the platform, both experimental and computational fluid dynamics (EFD and CFD) analyses will be used in the design cycle. The purpose of this work is to develop the CFD tools

* Research Scientist, MCAT Institute, Member AIAA.
† Research Scientist and Group Leader, Member AIAA.

for use in the SOFIA design.

The driven cavity problem has been a subject of much experimental research[2, 3] and numerical simulation of this class of problems has also been investigated by many researchers.[4-11] Komerath et. al[12] provided a review of open cavity research conducted during the past four decades. This work builds on past numerical studies by first validating the ability to predict shear layer and generic cavity flow fields,[2] including detailed numerical sensitivity studies, and then applying the code to both untreated and treated cavity SOFIA configurations. The treated cavity SOFIA computation also includes a model of the telescope. By comparing computed SOFIA flow fields to available experimental data,[1] we assess the capability to predict the characteristics of the untreated SOFIA configuration, and one of the proposed flow control designs. Prediction of the acoustic intensity levels and frequencies are of particular interest. If successful, this should develop the confidence required to use the developed CFD model in future SOFIA design studies. Efforts toward prediction of image distortion caused by the flow density variations are also be presented.

The following sections address the method used to predict the unsteady flows, including the modelling of turbulence, and the optical distortion. Results are presented for several two-dimensional cases and for two SOFIA configurations.

Numerical Methods

The objective of the numerical simulation of the flow about the SOFIA airborne observatory is to design a safe configuration which will have the least detrimental effects upon the optics. Towards this goal, the following transonic cavity flow problems were divided into three sections. First, the unsteady interaction of the external flow with the cavity requires time-dependent solutions to the Reynolds-averaged Navier-Stokes equations. Second, the shear layer growth rate is strongly dependent on turbulence effects which must be modelled due to the grid coarseness. Third, the optical model is applied to the unsteady density field.

Following discussion of the above models, boundary treatment and grid generation methods are presented.

Navier-Stokes Model

The algorithms used for this effort, coded by Buning and Chan,[13] are implemented within the Chimera overset grid framework.[14] The solutions were obtained using a diagonal scheme,[15] using spatially varying time steps for steady state computations, and fixed step size for unsteady flow simulations. The code utilizes the conventional dependent variable vector, $Q = [\rho, \rho u, \rho v, \rho w, e]^T$, and pseudo-finite-volume metrics. Euler implicit time marching and second-order spatial differencing was used for the computations presented here. Computations were performed on the Numerical Aerodynamic Simulator (NAS) Cray Y-MP 8/32 using SSD, at an expense of $14\mu s$/point/iteration.

Turbulence Model

Turbulence is modelled using the method of Baldwin and Lomax[16] modified with a variable F_{max} cutoff and a shear layer model. Viscous walls were specified such that the search for F_{max} terminated before leaving the boundary layer region. The eddy viscosity in the shear layer was computed as outlined by Buning.[13] However, for this effort σ_0 was set to 11.0 according to established experimental values.[17] In addition, previous numerical investigations appear to indicate that capture of the resonant frequencies is not strongly dependent upon the turbulence model in the cavity.[4, 8, 9]

Geometric Optics

The variation of the speed of light through gases is primarily a function of the density field. This fact has been extensively used to benefit the study of fluid physics, as exemplified by use of schlieren, shadowgraph, and interferometry techniques. The objective of this effort is to predict the distortion of an image caused by variations in the air density within the shear layer. Distortion is computed by using the history of the density variations within the shear layer to predict variations in the optical path length using geometric optics. This will in turn allow prediction of the minimum resolvable astronomical feature, and contribute to the telescope design specifications.

Geometric optics assumes that the impact of the fluid density on the optical field may be computed by casting light rays through a field discretized into tetrahedrons. Therefore, to utilize the simplifications afforded by the use of planar facets and piecewise continuous media, each hexahedron of the flowfield domain is tesselated into five tetrahedrons as shown in Fig. 2. Figure 3 depicts the modelling of a resulting planar interface, $\mathbf{p}(u, w)$, separating the media and the incident light ray, $\mathbf{q}_i(t)$.[18]

The problem can now be divided into three steps: 1) propagation of the ray, 2) intersection of the ray with a facet, and 3) refraction. Solution for the point contained in both the facet, $\mathbf{p}$, and the ray, $\mathbf{q}_i$, results in the intersection in parametric coordinates:

$$\mathbf{q}_i(t) = \mathbf{d} + \mathbf{e}t \;;\; \mathbf{p}(u, w) = \mathbf{a} + \mathbf{b}u + \mathbf{c}w$$

$$(\mathbf{b} \times \mathbf{c}) \cdot \mathbf{p} = (\mathbf{b} \times \mathbf{c}) \cdot \mathbf{q}_i$$

$$t = \frac{(\mathbf{b} \times \mathbf{c}) \cdot \mathbf{a} - (\mathbf{b} \times \mathbf{c}) \cdot \mathbf{d}}{(\mathbf{b} \times \mathbf{c}) \cdot \mathbf{e}}$$

$$u = \frac{(\mathbf{c} \times \mathbf{e}) \cdot \mathbf{d} - (\mathbf{c} \times \mathbf{e}) \cdot \mathbf{a}}{(\mathbf{c} \times \mathbf{e}) \cdot \mathbf{b}}$$

$$w = \frac{(\mathbf{b} \times \mathbf{e}) \cdot \mathbf{d} - (\mathbf{b} \times \mathbf{e}) \cdot \mathbf{a}}{(\mathbf{b} \times \mathbf{e}) \cdot \mathbf{c}}$$

Specification of the light ray origin and a direction initializes the problem. Following the search for the initial hexahedral cell in which the ray originates, the tetrahedron within this hexahedron must be computed. The shortest intersection distance of the ray with the 16 facets which compose the hexahedron determines the origin tetrahedron. Subsequent intersection and refraction processes are a marching procedure. The optical path length (OPL) is found from

$$OPL = \int n(s)ds \approx \sum_j n_j \Delta s_j$$

and variation of the OPL over the aperture gives a measure of the wavefront error caused by the shear layer.

The refraction process is determined according to Snell's law as shown in Fig. 3. Generalization to three dimensions is accomplished by rotation to the osculating plane, which includes the surface normal and both the incident and refracted rays. In this osculating plane, a rotated local coordinate system is defined:

$$\mathbf{q}_i = |\mathbf{q}_{i_n}|\hat{\mathbf{n}} + |\mathbf{q}_{i_t}|\hat{\mathbf{t}}$$

where

$$|\mathbf{q}_{i_n}| = |\mathbf{q}_i| \cos\theta_i \quad \text{and} \quad |\mathbf{q}_{i_t}| = |\mathbf{q}_i| \sin\theta_i$$

$$\hat{\mathbf{t}} = \frac{\hat{\mathbf{q}}_i - \hat{\mathbf{n}} \cos\theta_i}{\sin\theta_i}$$

Application of Snell's law $n_i \sin\theta_i = n_r \sin\theta_r$ where $n = 1 + \beta\frac{\rho}{\rho_{STP}}$ results in an expression for the refracted ray:

$$\hat{\mathbf{q}}_r = \hat{\mathbf{n}} \cos\theta_r + \hat{\mathbf{t}} \sin\theta_r$$

The local index of refraction, n_j, is found by arithmetically averaging the densities at the four vertices of the tetrahedron. The Gladstone-Dale constant, β, is a function of the media and of the wavelength. Using air as the media and a wavelength of $\lambda = \lambda_D = 5893\text{Å}$, then $\beta = 2.92 \times 10^{-4}$. The wavelengths of interest for SOFIA range from the near infrared, 1μm, to the microwave, 1 mm. Optical distortion is more severe for shorter wavelengths, hence the choice of yellow sodium light, λ_D.

Finally, to obtain a measure of the loss in irradiance due to the fluctuating density field, the OPL for vacuum conditions is subtracted from the OPL through the gas to yield the optical path difference (OPD). The value of $\text{OPD}|_{rms}$ is computed using a sequence of OPD's at a fixed station. Using the rms wavefront distortion (σ), the phase distortion (Φ) is found from $\Phi = \frac{2\pi\sigma}{\lambda}$. The Strehl ratio, given by $\frac{I}{I_0} = e^{-\Phi^2}$, is a measure of the peak intensity to which a beam can be focused. The computational expense of the procedure outlined above is currently 250μs/hexahedron/ray on the NAS Cray 2.

Boundary Conditions

The viscous impermeable wall conditions are no-slip, zero normal pressure gradient, and adiabatic. Information transfer across overset mesh boundaries is implemented using non-conservative trilinear interpolation of Q. Treatment of the farfield boundaries is case dependent and is noted in the results section.

Geometry Treatment

A discussion of the treatment of the surface, the grid topology, and the grid strategy is given below.

Surface Modelling

The geometry used for the SOFIA configurations utilized clipped wings to emulate the experiment. The use of clipped wings in the wind tunnel test allowed a cavity of more realistic size to be studied. The fuselage, wing, fairing, nacelles, and telescope geometry were obtained from CAD databases. Positioning errors in the database were corrected using blueprints.

The acquisition of the quiet configuration (100) aperture grid warrants additional comment. Wind tunnel testing resulted in a hand-formed ramp and aperture (see Fig. 19) which was subsequently laser digitized.[19] This data, accurate to approximately 0.2 mm, was then converted into a form suitable for the surface grid.[20]

Surface definition via bicubic surfaces in regions of high curvature can cause local oscillatory behaviour.[18, 21] Along overlapping surfaces this property is manifested as C^0 discontinuities at zone boundaries. The problem is ameliorated through bilinear projection from one zone boundary to another.[22] The distance of projection is typically five orders of magnitude less than a characteristic geometry length.

Topology

The overset grid topology scheme was chosen for its geometric flexibility and its ability to allow refinement of individual zones. The use of a different grid for each component of the geometry simplifies changes that will occur as the design matures. In fact, the geometries with cavities were built upon the clean configuration grids, providing a savings of many man-hours. The topology was chosen to allow rapid evaluation of new configurations and permit simple specification of turbulent wall and shear layer regions.

Grids

The grids for these simulations were obtained via algebraic[21] and hyperbolic[23] means, the topology was chosen to allow the use of these grid generation methods. Generally a wall spacing of $y^+ = 4.0$ was estimated for the viscous walls, the farfield boundary was

placed at 20 fuselage diameters, and the outflow 10 diameters downstream. Damping of acoustic waves at the farfield boundary was achieved by the use of large cells which were unable to support the wave.

The clean configuration, without a cavity, was modelled using four grids for the half-body: the fuselage, wing, wing tip, and nacelle. The grid point count was approximately 4×10^5. The fuselage grid was refined in anticipation of the cavity to provide similarly sized cells in interpolation regions.

The untreated aperture geometry, configuration 25 of the wind-tunnel test, was gridded by reflecting the grids from above and adding two for the cavity. The fuselage zone boundaries were shifted meridionally to move interpolation away from the cavity region. The two additional grids consisted of an outer cavity grid surrounding the cavity region and an inner cavity grid which included the cavity walls and the shear layer region. The outer zone was utilized to isolate the cavity unsteadiness from the global solution. The total grid point count was about 1.2×10^6 distributed in 10 zones.

The treated aperture geometry, configuration 100 of the wind-tunnel test, was modelled by addition of seven grids to the clean case: isolation, aperture wall, shear layer, cavity wall, telescope tub, secondary mirror, and an inner ramp grid. The total grid point count was about 1.8×10^6 in 15 zones.

Results and Discussion

Validation of the code was accomplished by evaluation of two- and three-dimensional cases. Numerical results for free shear layer and rectangular two-dimensional cavity flows were compared with analytic and experimental data to evaluate the capability of capturing the fundamental physics. Analysis of the SOFIA configuration simulations, including evaluation of optical distortion is also presented.

Free Shear Layer

A series of numerical experiments were performed using a two-dimensional shear layer as the test case. Sensitivities of mean and time-varying quantities to changes in time step size, fourth-order dissipation levels, and grid refinement were determined. Additionally, partial validation of the algebraic turbulent shear layer model was determined through comparison with similarity solutions and experimental data.

The computational domain for this case includes a two inch splitter plate embedded in a channel, with initial conditions specified as a discontinuous step at the channel centerline. The channel extends 30 inches downstream of the splitter plate trailing edge, and five inches above and below the plate. Inviscid walls were specified for three inches upstream of the splitter plate and for the channel walls. The inflow and outflow conditions were implemented using one-dimensional characteristic relations holding mass flow, total enthalpy, and flow angle fixed at the inlet, and fixing pressure at the exit plane. The boundary layers on the splitter plate and the shear layer were turbulent. Reynolds number based on the mean velocity of the streams and the length of the splitter plate was 6.7×10^5.

The results for three grid refinement levels are shown in Fig. 4 along with Görtler's similarity solution. The velocity profiles are taken 10 inches downstream of the trailing edge of the plate. The solution can be seen to become grid dependent when the grid becomes coarser than approximately 20 points across the layer. The Mach ratio for this case was 0.2/0.8 and $\sigma = 20.7$. Eddy viscosity was observed to grow linearly in accordance with the Clauser formulation.

Numerical experiments to determine the dependence of p_{rms} on the level of fourth-order dissipation showed that a change in fourth-order smoothing from 0.01 to 0.05 caused a change of less than 1% in sound pressure level.

The velocity ratio across the SOFIA cavity shear layer will vary with streamwise location. Hence, comparison of the variation of spread rate with velocity ratio is shown in Fig. 5. The spreading parameter σ originates from the similarity solution shown in Fig. 4 and is inversely related to the spread rate, db/dx. The value of the spreading parameter when the velocity of one of the streams is zero is σ_0. Three velocity ratios are shown for low Mach numbers with about 20 points maintained across the layer for all cases. The computed spreading rates are within the bounds of the experimental data.[17]

Two-Dimensional Cavity

The objective of this two-dimensional cavity case was to demonstrate the prediction of self-induced cavity resonance. Validation data is provided by comparison against Rossiter's experiment.[2] Sensitivity of the solution to topology, second-order dissipation, and turbulence model effects were determined.

The cavity geometry and grid topology is shown in Fig. 6, where the grid has been coarsened for clarity. The test conditions were set as:

$$M_\infty = 0.9 \quad Re_L = 1.47 \times 10^6$$
$$L = 8in.$$

The ratio of cavity length by depth (L/D) was 2 for this model. The inflow boundary was placed 7.5 L upstream of the cavity leading edge, the outflow boundary 4.5 L downstream of the cavity trailing edge. The inflow and outflow conditions were specified as for the free shear layer cases, and an inviscid wall was placed 5 L above the cavity.

Figures 7 and 8, respectively, depict instantaneous Mach and pressure contours obtained during the computation in which the time step size was $\Delta t = 1.97\mu s$. Inspection of the contours across zone boundaries indicate that the interpolation process is well-behaved for this unsteady flow. The Mach contours show the oscillatory shear layer behaviour which is present for this case. The pressure contours depict the feedback mechanism forwarded by Rossiter. Briefly, the cycle begins with the propagation of a wave from the aft wall of the cavity to the forward face. Wave reflection from the forward wall causes the shear layer to bow outwards, shedding vorticity. The deflected shear layer convects downstream and induces another cycle. The frequencies at which this feedback is reinforced is determined by ambient temperature and Mach number.

The pressure histories along the cavity walls are depicted in Fig. 9. Comparison of Rossiter's data to present results, shown as power spectral density (PSD) in Fig. 10, indicate agreement in frequency at the peak magnitudes. Magnitudes are higher for the present case by about 2 dB, however for this experiment and other numerical work this has been observed as an effect of width. In these studies,[2, 9] the sound level was found to be inversely related to L/W; the cavity for Rossiter's experimental work was of $L/W = 2$. The PSD for this case was computed using 8192 time samples, no zero-padding, and a square window.

Variation of the second-order dissipation, ϵ_2, from 0.5 to 0.3 caused no discernable change in the pressure histories. Additionally, in order to test a hypothesis of a limited domain of unsteadiness, an isolation zone was implemented as shown in Fig. 6. The flow outside the zones of interest was frozen, resulting in a decrease of the cavity sound pressure levels by 2%. A final comparison between experimental data and numerical results is provided in Fig. 11, where the variation of the mean and oscillatory pressures along the cavity walls is shown. Given the difference in spatial dimensions and turbulence modelling uncertainties, the trends appear reasonable for a flow of this complexity.

Clean Configuration

In order to provide a measure of validation, the geometry and flow conditions were chosen to replicate the wind tunnel tests:

$$M_\infty = 0.85 \quad Re_L = 4.2 \times 10^6$$
$$L = 12.6in. \quad \alpha = 2.5^\circ$$

Subsequent correction of the wind tunnel data has resulted in the $Re_L = 4.0 \times 10^6$, about 5% lower than above. The temperature difference from this correction causes the sound speed in these computations to be approximately 6% higher than experiment. Numerical results obtained for this 7% scale model are discussed below.

The wind tunnel model without cavity was simulated in order to assess angle of attack errors owing to wind-tunnel wall effects. Figure 12 compares the present pressure coefficient profiles along the crest, side, and bottom of the model with flight data[24] and wind tunnel results.[1] Experimental results are shown for both untripped and tripped cases, the latter case was used for all subsequent wind tunnel testing. Although this comparison indicates that the influence of the tunnel wall was small near the cavity, pressures along the bottom of the model are shifted, possibly from due to the effect of the lower wall. A four-order drop in magnitude of $\delta\rho|_\infty$ was attained for this steady case.

Configuration 25

The geometry shown in Fig. 13 was the initial cavity configuration tested in the wind tunnel. This simulation was implemented in order to demonstrate the capture of self-excited cavity resonance in three-dimensions. The flow conditions were the same as used above, the flowfield was initialized from the steady clean case. The stability-limited time step size used was $\Delta t = 3.53\mu s$. This interval size corresponds to a $\nu \approx 1$ in the streamwise direction within the shear layer, and a $\nu_{max} \approx 500$.

Instantaneous Mach number contours in Fig. 14 show the flapping of the shear layer and interpolation treatment. Sample pressure histories on the cavity walls are shown in Fig. 15. Comparison of the PSD resulting from the wind tunnel and numerical efforts are shown in Fig. 16. The PSD was obtained using 2048 points, a Hanning window, and no zero-padding. The predicted frequencies of the dominant tones appear reasonable, and the dominant tone is within 3 dB of experiment. The magnitudes of the higher modes are much lower than found experimentally.

Estimation of the grid resolution required to maintain a propagating wave of proper magnitude can be deduced from the two-dimensional cavity and configuration 25 results. First, wavelength can be estimated by assuming the wave to be harmonic at a given frequency and travelling at the local speed of sound. Next, it is noted that frequencies of 2 kHz were resolved well in the two-dimensional case, in which the grid resolution was such that about 40 points supported the wave. From the configuration 25 results, it is seen that only the 700 Hz peak is well resolved, which again gives approximately 40 points across the wave for this coarser grid. Although numerical damping of the higher frequencies can be expected, most of the energy is contained in the lowest frequency mode, as can be seen in the SPL comparison of Fig. 17. The SPL for the resonating and quieted geometries ob-

tained numerically are in reasonable agreement with experiment.

Configuration 100

This simulation was implemented in order to determine if the same level of quieting would be predicted numerically as was found experimentally. Previous investigations[12] of cavity noise suppression has shown aft ramp treatments to be effective, possibly by allowing a stable shear layer reattachment site. For the SOFIA experiment, this type of geometry treatment was found to be quieter than the untreated configuration 25 case by over 30 dB. Figure 17 shows that the proper trend is computed. The flow conditions were again initialized from the clean case. The stability-limited time step size used was $\Delta t = 7.06\mu s$. The PSD was obtained using 4096 points, a Hanning window, and no zero-padding.

Figure 18 shows the position of the telescope in the aircraft and the coarsened telescope grids. Figure 19 depicts the aft ramp treatment modelled for this case along with computed particle traces, and Fig. 20 shows the topology used in the cavity region, where the grids have been coarsened for clarity. Figure 21 depicts mean experimental and computational shear layer Mach profiles. The vertical scale of the profiles is twice that shown in the contour plot for clarity. Note that the experimental profiles were obtained using a rake, which is sensitive only to u, the x-component of velocity. The discrepancy between $|u|/c$ and $|\mathbf{V}|/c$ is approximately 0.05 at the lower speed end of the profile. Figure 21 indicates reasonable agreement for growth rates, though the profile shapes become quite different as the shear layer approaches the ramp. This discrepancy may be in part due to probe position uncertainty and geometry modifications to allow for the probe mechanism. These modifications included removal of the telescope assembly and cutting a streamwise slot in the ramp. Time averaging of velocities were performed over 1000 time steps and profiles were insensitive to segment length.

Figures 22 and 23 show the pressure history and resultant PSD on the cavity walls. Although the peak spectra levels are in agreement, the spectra levels can again be seen to drop more rapidly with frequency for the numerical than experimental results. The pressures on the primary mirror, shown in Figs. 24 and 25, show lower high frequency content with the peak at 1800 Hz not resolved. Figures 26 and 27 show a low frequency component which was not found experimentally. The discrepancy is manifested as the SPL difference seen in Fig. 17.

Aero-optics

Application of the geometric optics code to two preliminary test cases were undertaken to determine the sensitivity of the code to tesselation, which is non-unique. The parallel emergence of the rays after propagation through a plate and a prism of $n = 2.4$ suggests that the results are relatively insensitive to the method of tesselation.

The optics code was applied to the density field obtained from configuration 100 from $t = 0$ to $7.8ms$ as depicted in Fig. 28. Ten rays were propagated through 110 density fields in time intervals of $\Delta t = 70.6\mu s$. The results shown here are for a computational plane at approximately the cross flow center of the aperture (Fig. 28), which will provide only a streamwise variation in optical properties. The results are presented compared to experiment and previous analysis[25] in Fig. 29. Two computed results are shown, one result with rays originating immediately below the shear layer ($r_0 = 10.8$"), and the other plot for rays originating below the secondary mirror ($r_0 = 7.8$"). Shear layer aerodynamic measurements[1] were used to determine distortion for the experimental data shown in Fig. 29 while the analytic result assumes an index-matched shear layer with a sinusoidal n profile.[25]

Figure 29 shows that the distortion model applied through the shear layer alone ($r_0 = 10.8$") underpredicts the data determined analytically and experimentally. However, the computed trend is generally consistent with the data. Comparison of the computed results for $r_0 = 7.8$" and 10.8" shows an increment in OPD. This distortion increment appears to be caused by a jet of fluid resulting from the impingement of the shear layer on the aft ramp. The dip in the $r_0 = 7.8$" results at $x = 42$" is caused by the presence of the secondary mirror, in which n was defined to be unity.

Conclusions

The work presented here is the initial effort towards development of a design and analysis tool for use throughout the SOFIA project life. Thus far, this investigation has demonstrated that self-induced cavity resonance can be accurately captured for complex geometries modelled using an overset mesh topology. Shear layer profiles and resonant behaviour are consistent with previous analytic and experimental work. Generally, sound pressure levels agree to within 4%. Topology treatment has allowed the simple specification of turbulent wall and shear layer regions as well as providing a means of isolating the unsteady flow region.

The geometric aero-optical model shows proper trends, but the distortion magnitude is underpredicted. Further investigation is required to determine if improved wavefront distortion results can be achieved.

Improvements in the energy distribution in frequency may be attained by use of a higher-order spa-

tial stencil or more simply by grid refinement. The use of higher order turbulence models should also be investigated. Improvements in the optical modelling should include an empirical model to account for scattering owing to subgrid turbulent scales.

References

[1] Rose, W.C., and Cooley, J.M.,"SOFIA Wind Tunnel Data Analysis and Implications for the Full-Scale Aircraft," Rose Eng. and Research, Inc., Dec. 1990.

[2] Rossiter, J. E., "Wind-Tunnel Experiments on the Flow Over Rectangular Cavities at Subsonic and Transonic Speeds," Royal Aircraft Establishment Reports and Memoranda No. 3438, Oct. 1964.

[3] Neary, M.D.,"Time Dependent Self-Sustaining Oscillations of Cavity Flow," AIAA-87-0142, Jan. 1987.

[4] Hankey, W.L., and Shang, J.S.,"Analysis of Pressure Oscillations in an Open Cavity," *AIAA J.*, Vol. 18, Aug. 1980. pp. 892-898.

[5] Venkatapathy, E., Lombard, C.K., and Nagaraj, N.,"Numerical Simulation of Compressible Flow Around Complex Two-Dimensional Cavities," AIAA-87-0116, Jan. 1987.

[6] Om, D., "Navier-Stokes Simulation for Flow Past an Open Cavity," *AIAA J. of Aircraft*, Vol. 25, Sept., 1988, pp. 842-848.

[7] Dougherty, N.S., Holt, J.B., Nesman, T.E., and Farr, R.A.,"Time-Accurate Navier-Stokes Computations of Self-Excited Two-Dimensional Unsteady Cavity Flows," AIAA-90-0691, Jan. 1990.

[8] Suhs, N.E.,"Computations of Three-Dimensional Cavity Flow at Subsonic and Supersonic Mach Numbers," AIAA-87-1208, Jun. 1987.

[9] Rizzetta, D. P., "Numerical Simulation of Supersonic Flow Over a Three-Dimensional Cavity," *AIAA J.*, Vol. 26, Jul. 1988. pp. 799-807.

[10] Baysal, O., and Stallings Jr., R.L.,"Computational and Experimental Investigation of Cavity Flowfields," AIAA-87-0114, Jan. 1987.

[11] Löhner, R.,"Three-Dimensional Fluid-Structure Interaction Using a Finite Element Solver and Adaptive Remeshing," *Computing Systems in Eng.* 1, Nos. 2-4, 1990. pp. 257-272.

[12] Komerath, N.M., Ahuja, K.K., and Chambers, F.W.,"Prediction and Measurement of Flows Over Cavities - A Survey," AIAA-87-0166, Jan. 1987.

[13] Buning, P.G., and Chan, W.M.,"OVERFLOW/F3D User's Manual, Version 1.5," NASA/ARC. Nov. 1990.

[14] Benek, J.A., Buning, P.G., and Steger, J.L., "A 3-D Chimera Grid Embedding Technique," AIAA-85-1523, Jul. 1985.

[15] Pulliam, T.H., and Chaussee, D.S.,"A Diagonal Form of an Implicit Approximate-Factorization Algorithm," *J. Comp. Phys.*, Vol. 39, Feb. 1981. pp. 347-363.

[16] Baldwin, B.S., and Lomax, H., "Thin-Layer Approximation and Algebraic Model for Separated Turbulent Flows," AIAA-78-257, Jan. 1978.

[17] Birch, S.F. and Eggers, J.M.,"A Critical Review of the Experimental Data for Developed Free Turbulent Shear Layers," *Free Turbulent Shear Flows*, NASA SP-321, July 1972.

[18] Atwood, C.A., and Vogel, J.M.,"Surface Grid Generation for Flowfield Applications Using B-Spline Surfaces," AIAA-89-2177, Aug. 1989.

[19] Merriam, M.L., and Barth, T.J.,"3-D CFD in a Day: The Laser Digitizer Project," AIAA-91-1654, Jun. 1991.

[20] Vaillancourt, K., Private communication.

[21] Steinbrenner, J.P., Chawner, J.R., and Fouts, C.L., "A Structured Approach to Interactive Multiple Block Grid Generation," AGARD FDP Specialists Mtg. on Mesh Generation for Complex Three-Dimensional Configurations, Loen, Norway, May 1989.

[22] Parks, S.J., Buning, P.G., Steger, J.L., and Chan, W.L.,"Collar Grids for Intersecting Geometric Components within the Chimera Overlapped Grid Scheme," AIAA-91-1587, Jun. 1991.

[23] Chan, W.L., and Steger, J.L.,"A Generalized Scheme for Three-Dimensional Hyperbolic Grid Generation," AIAA-91-1588, Jun. 1991.

[24] Haslund, R.L.,"SOFIA Viewport Configuration Wind Tunnel Test Report," Boeing Aerospace and Electronics Sensors Technology, Oct. 1988.

[25] Bogdanoff, D.W., "The Optical Quality of Shear Layers: Prediction and Improvement Thereof," *AIAA J.*, Vol. 22, Jan. 1984. pp. 58-64.

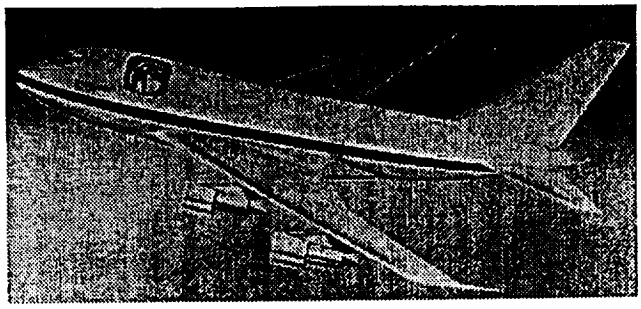

Fig.1 Artist's concept of the SOFIA configuration

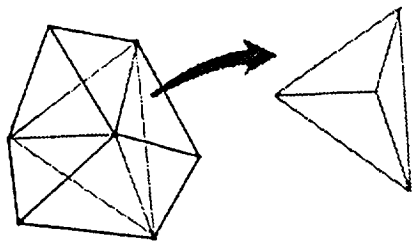

Fig.2 Tesselation of hexahedrons into tetrahedrons

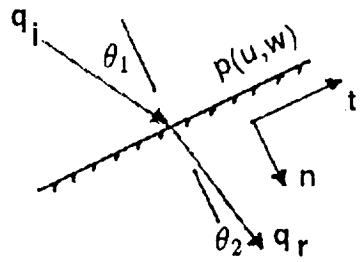

Fig.3 Intersection and refraction procedure

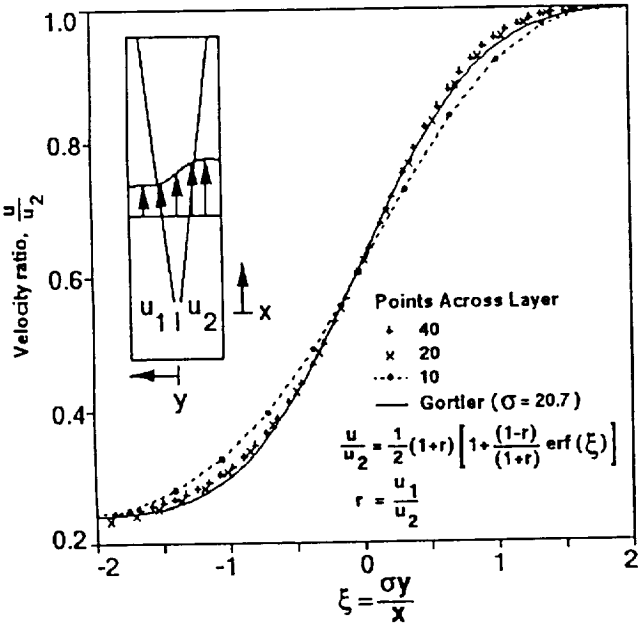

Fig.4 Velocity profiles of differing grid resolution compared to similarity

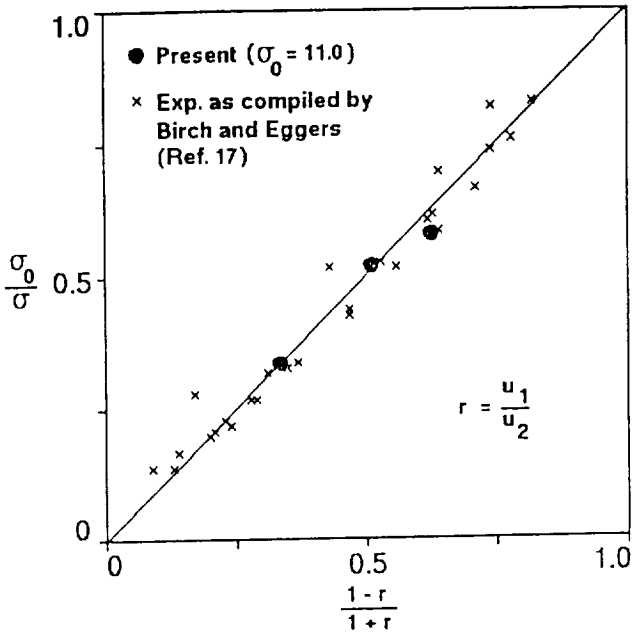

Fig.5 Variation of spread rate with velocity ratio

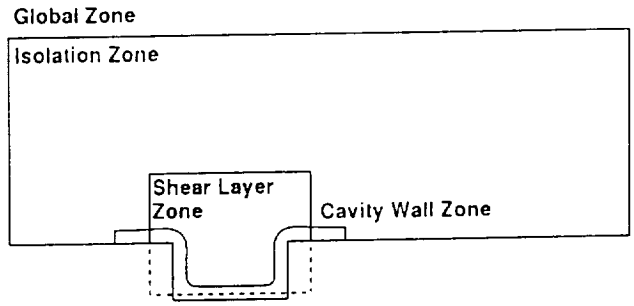

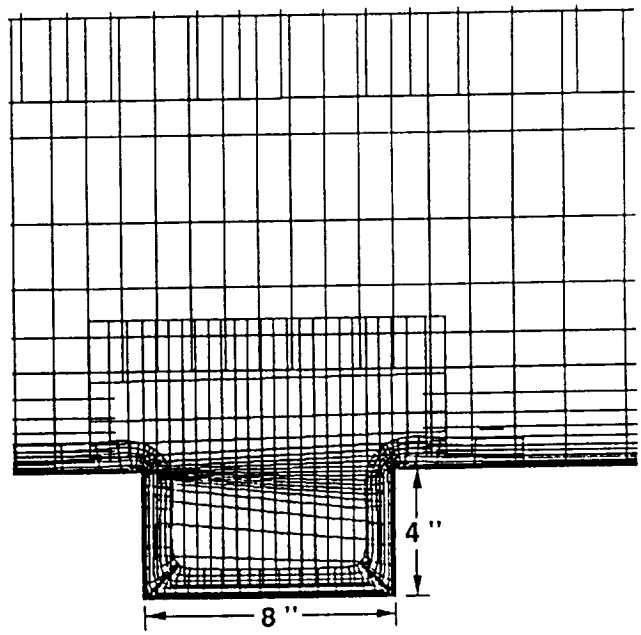

Fig.6 2-d cavity: Topology and grids

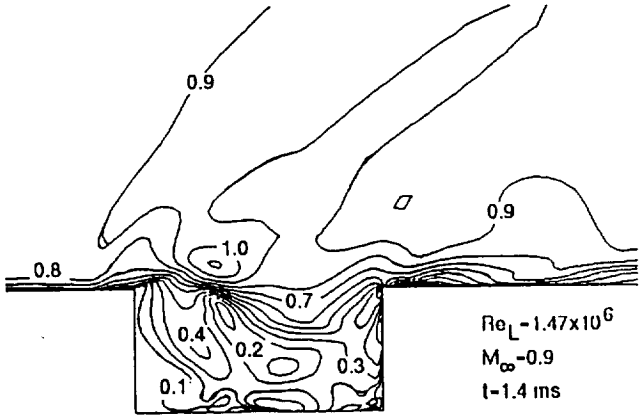

Fig.7 2-d cavity: Instantaneous Mach contours

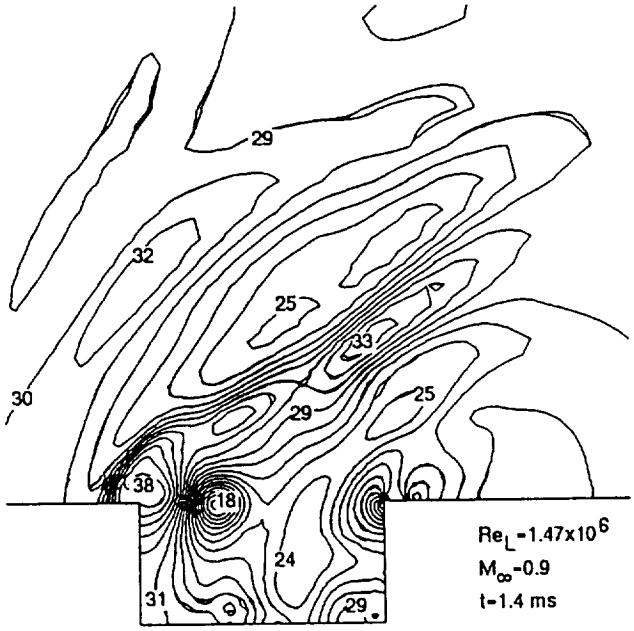

Fig.8 2-d cavity: Instantaneous pressure contours

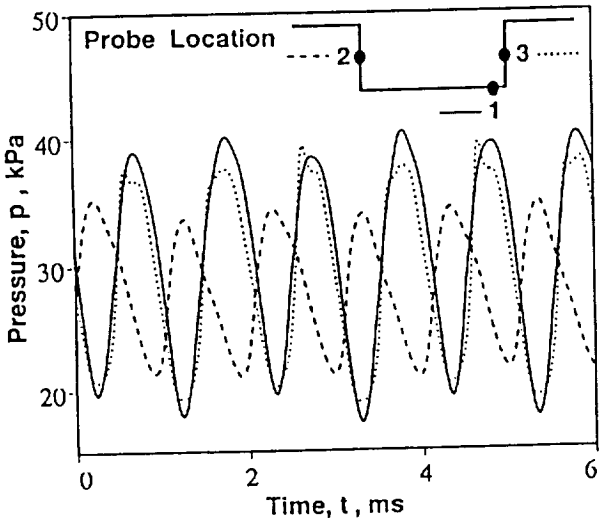

Fig.9 2-d cavity: Pressure history

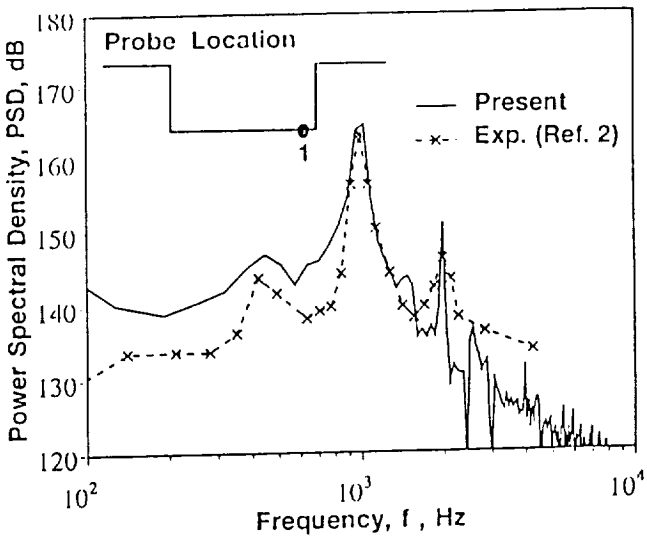

Fig.10 2-d cavity: Power spectra comparison

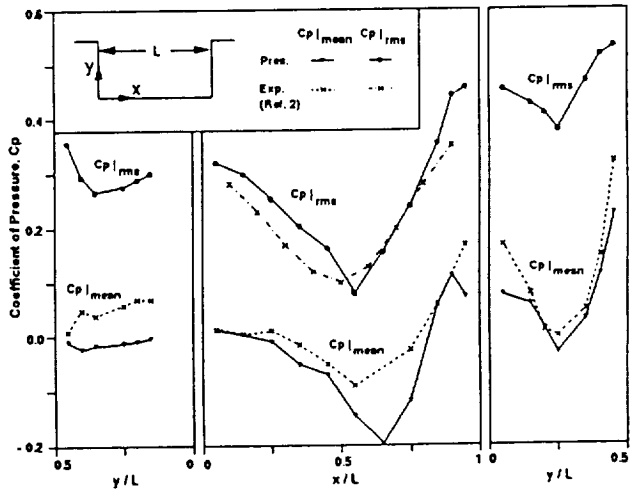

Fig.11 2-d cavity: Variation of mean and oscillatory pressures

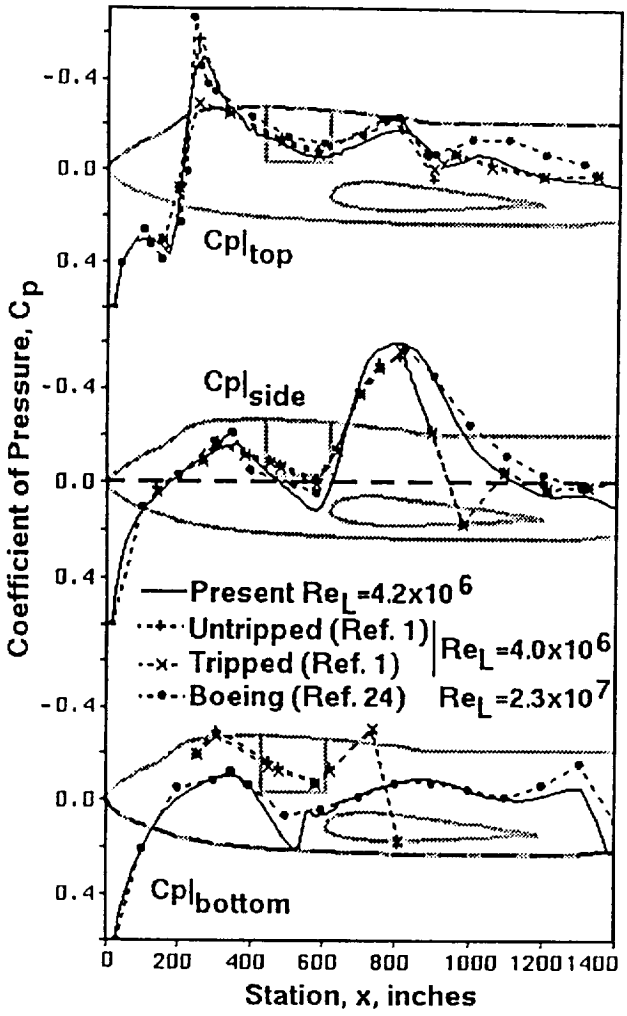

Fig.12 Clean configuration: Pressure coefficient comparison

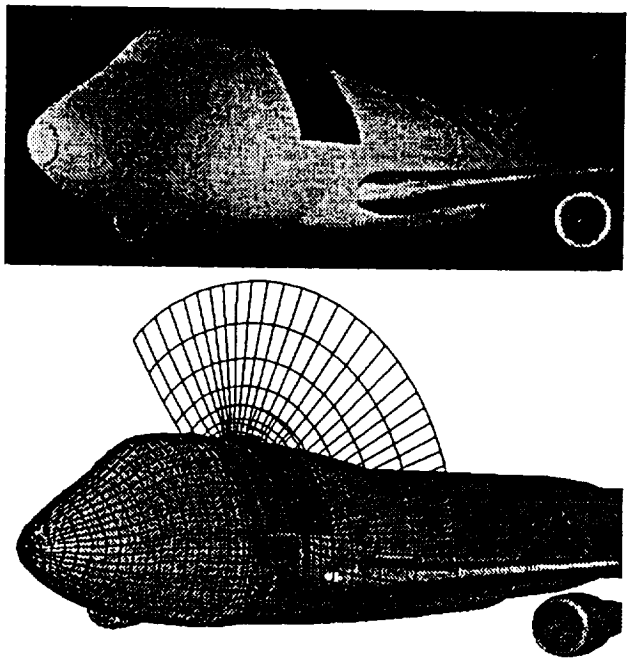

Fig.13 Configuration 25:Wind tunnel and numerical models

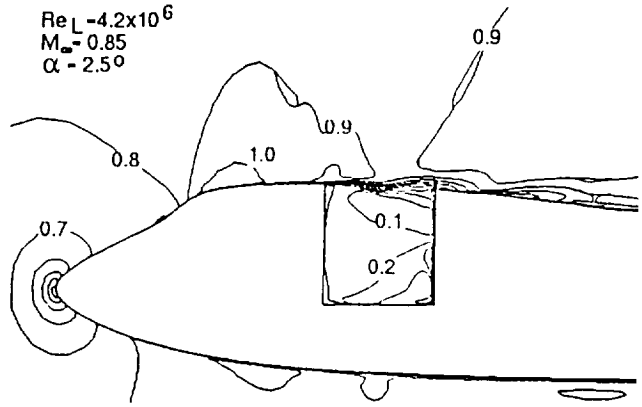

Fig.14 Configuration 25:Mach contours at y=0

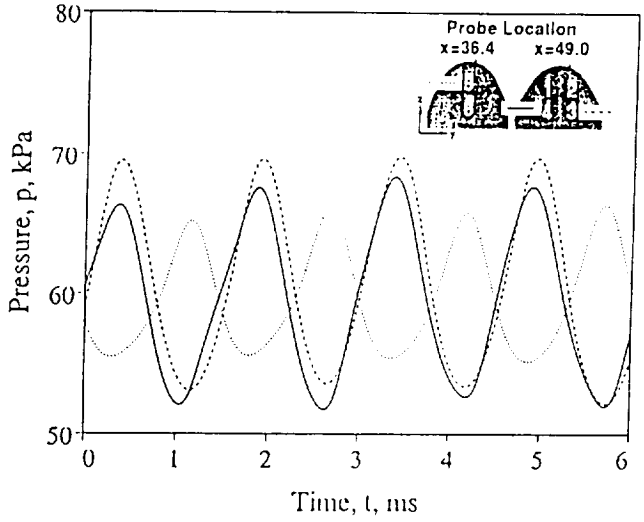

Fig.15 Configuration 25: Pressure histories

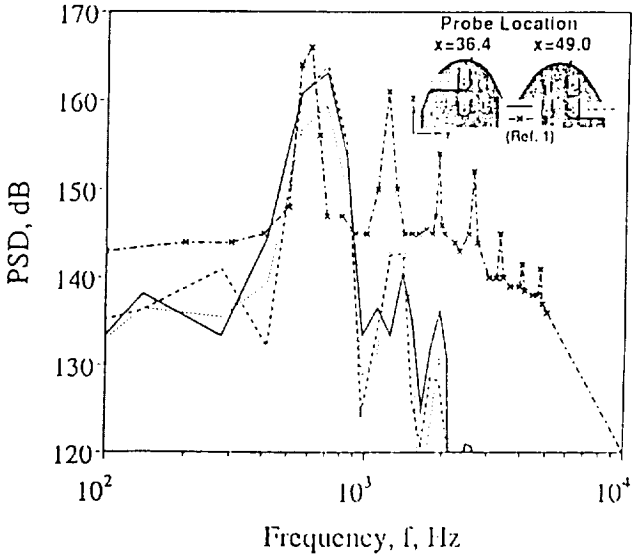

Fig.16 Configuration 25: Power spectra

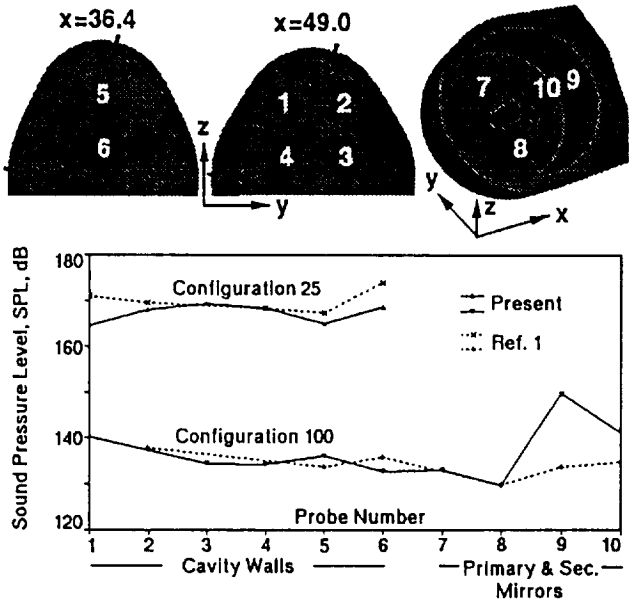

Fig.17 Comparison of sound pressure levels

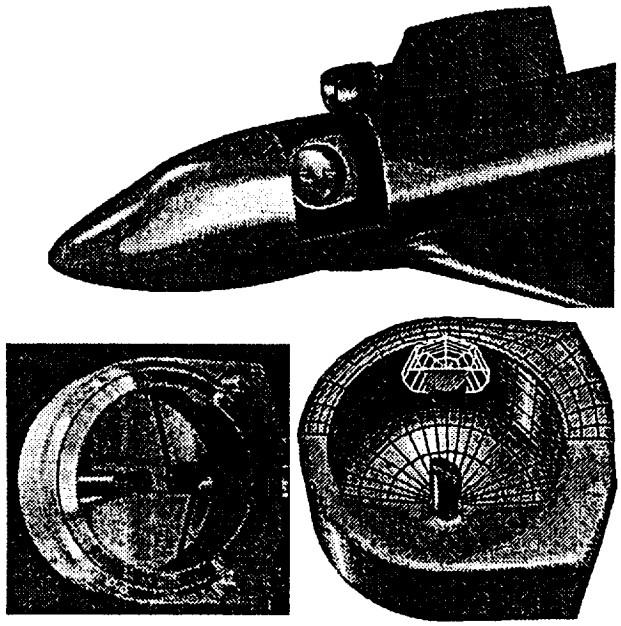

Fig.18 Telescope location and grids

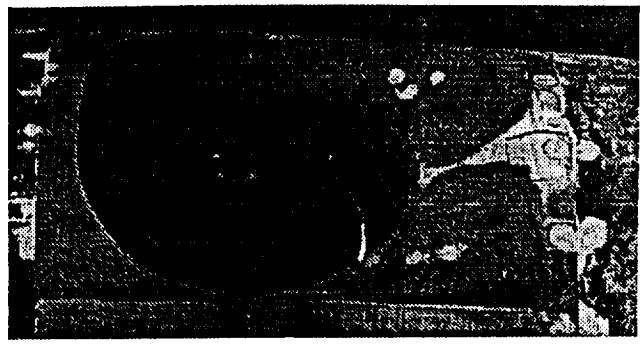

Fig.19 Configuration 100: Treated aperture

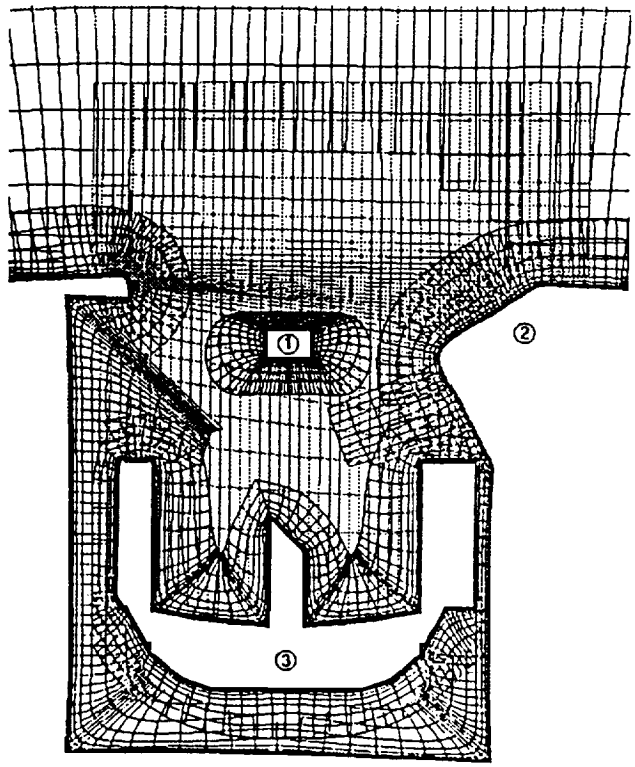

① Secondary Mirror
② Aft Ramp
③ Primary and Tertiary Mirror Assembly

Fig.20 Configuration 100: Cavity region topology

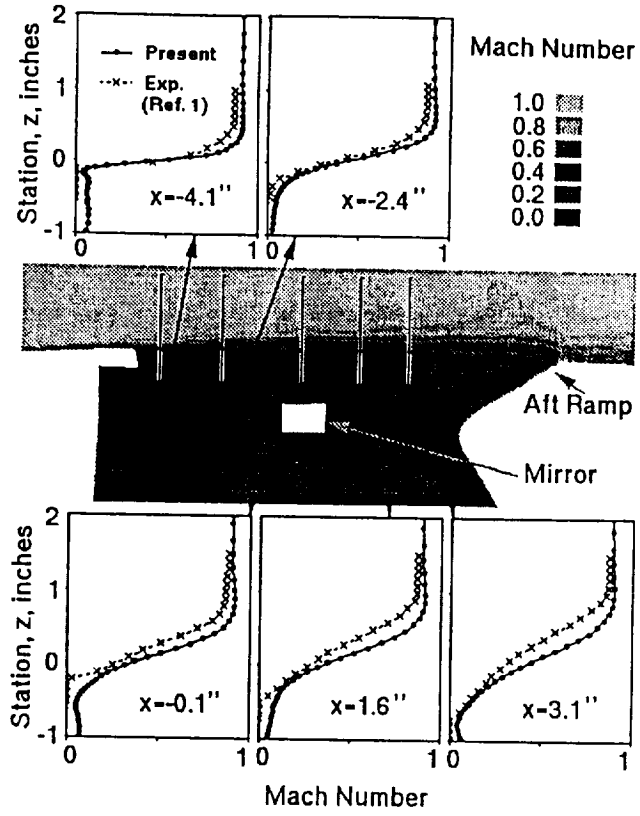

Fig.21 Configuration 100: Mean Mach profiles

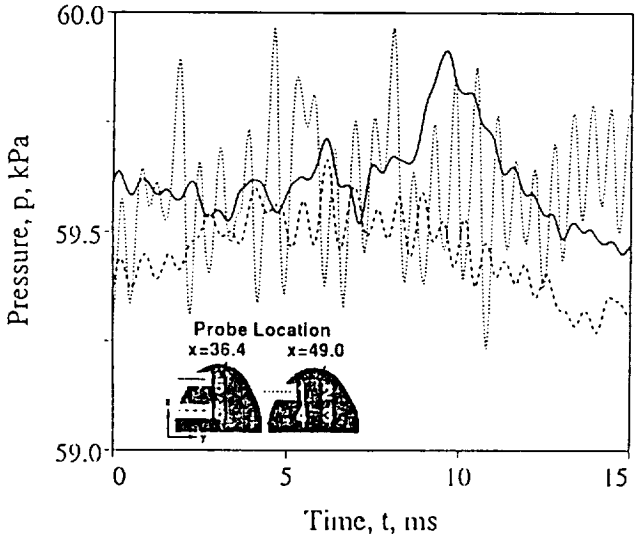

Fig.22 Configuration 100: Pressure history on cavity wall

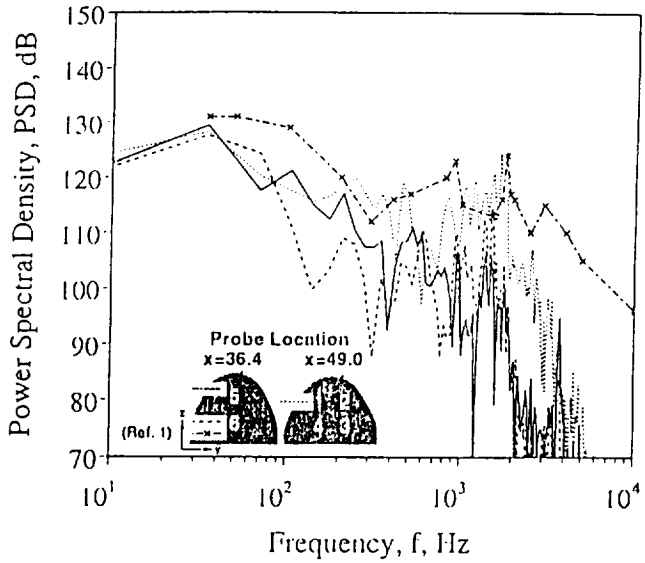

Fig.23 Configuration 100: PSD on cavity wall

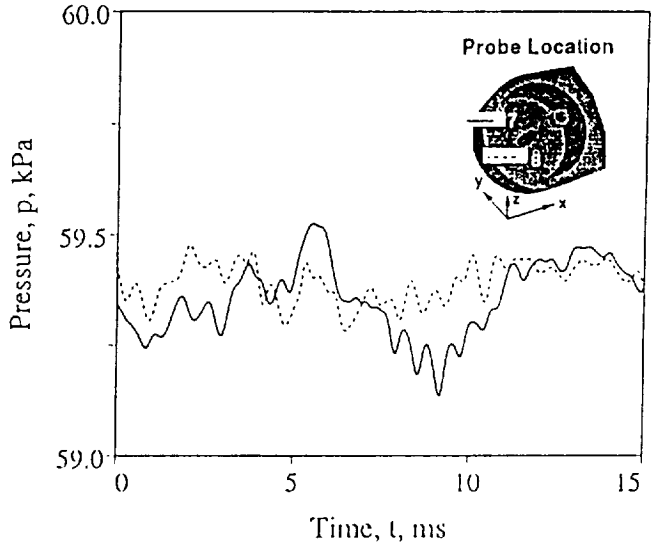

Fig.24 Configuration 100: Pressure history on primary mirror

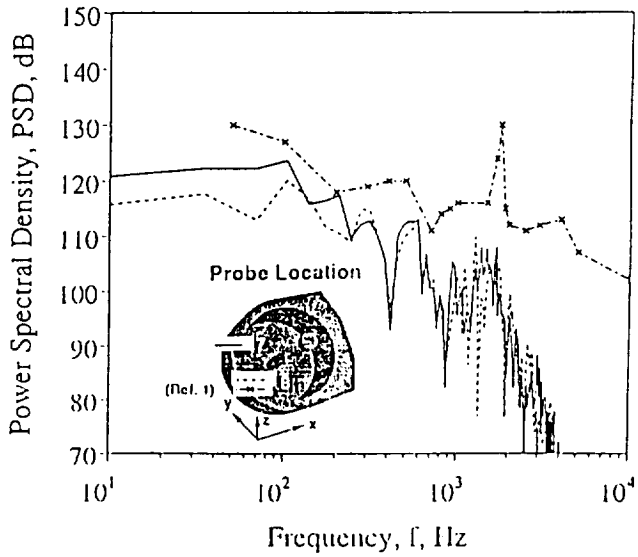

Fig.25 Configuration 100: PSD on primary mirror

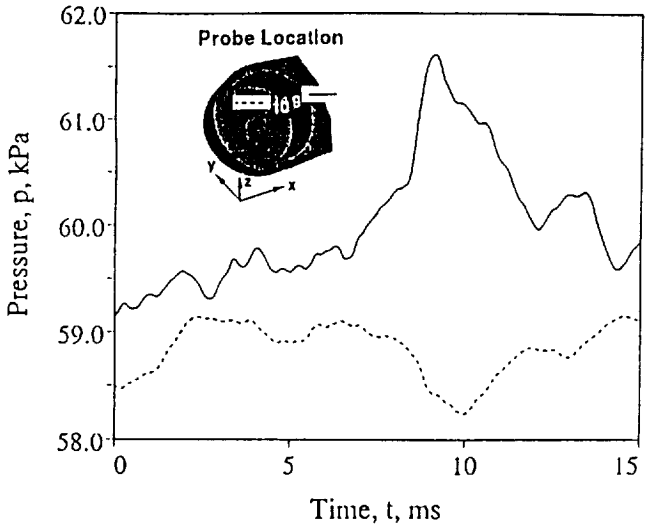

Fig.26 Configuration 100: Pressure history on secondary mirror

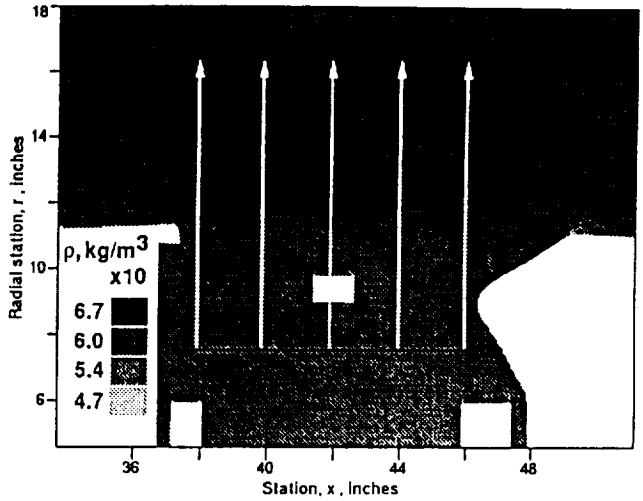

Fig.28 Optical refraction model

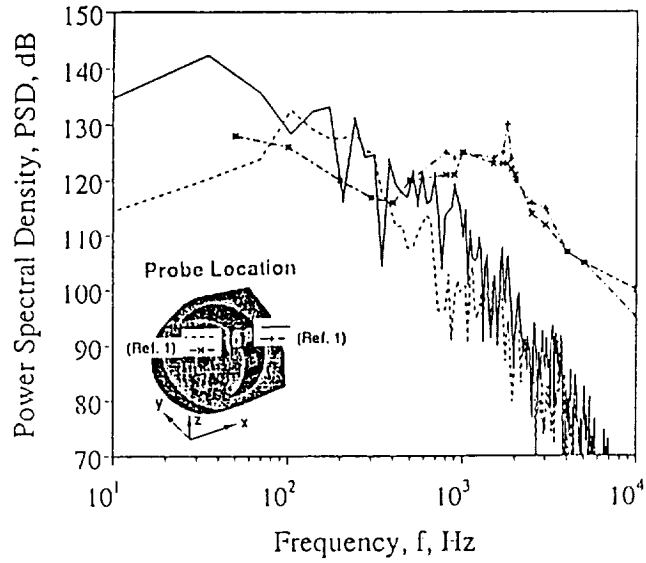

Fig.27 Configuration 100: PSD on secondary mirror

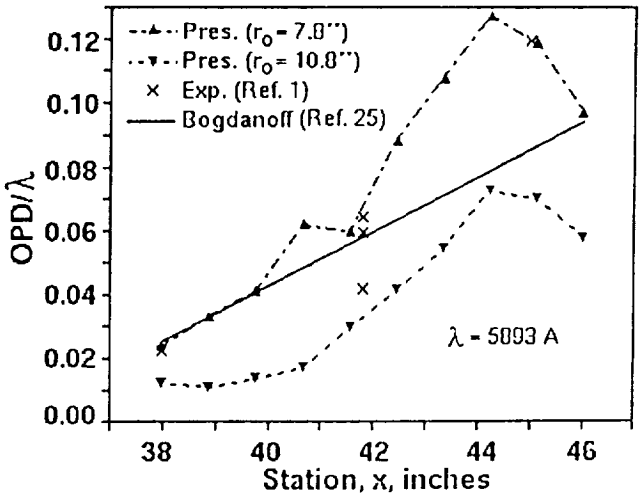

Fig.29 Comparison of wavefront distortion